Thermal Management in AlGaAs-On-Insulator Microresonators

Enabling and Extending Soliton Comb Generation

Zhao, Yanjing; Ye, Chaochao; Liu, Yang; Zhou, Yueguang; Yvind, Kresten; Pu, Minhao

Published in:
Laser and Photonics Reviews

Link to article, DOI:
10.1002/lpor.202401223

Publication date:
2025

Document Version
Peer reviewed version

LASER & PHOTONICS REVIEWS
www.lpr-journal.org

Thermal Management in AlGaAs-On-Insulator Microresonators: Enabling and Extending Soliton Comb Generation

*Yanjing Zhao, Chaochao Ye, Yang Liu, Yueguang Zhou, Kresten Yvind, and Minhao Pu**

Dissipative Kerr solitons offer a promising approach for integrated frequency comb sources. Although aluminum gallium arsenide (AlGaAs) exhibits ultrahigh nonlinearity, its strong thermo-optic effect raises significant challenges for stable soliton generation. Triggerring solitons necessitates either cryogenic cooling or resonator engineering, imposing stringent requirements on operational environments, comb spacing, and bandwidth. In this work, thermal management in AlGaAs-on-insulator microresonators is addressed using an auxiliary laser. This approach effectively suppresses the adverse thermal resonance shifts, thus enabling room-temperature soliton comb generation. Simultaneously, the residual thermal effects can be leveraged to expand the soliton existence range up to 37 GHz without active feedback. The scheme imposes no limitations on resonator parameters, facilitating the observation of near-zero-dispersion solitons. This broadens the exploration horizons on the AlGaAsOI platform. The extended soliton existence range ensures a stable and robust soliton operation, which is crucial for fully exploiting the ultra-high effective nonlinearity and high optical quality factors exhibited by this platform. This advancement is poised to accelerate the practical deployment of AlGaAs frequency comb sources.

1. Introduction

Optical frequency combs have significantly advanced precision time and frequency metrology[1] with broad applications like spectroscopy,[2] optical clocks,[3,4] optical communications[5] and range measurement.[6] Microresonator-based dissipative Kerr solitons (DKS) pave the way for miniaturized frequency combs, extending their utility beyond laboratory.[7–9] Such DKSs have been demonstrated in various material platforms, including silicon nitride,[10] silica,[11] aluminum nitride,[12] silicon carbon,[13] chalcogenide[14] and lithium niobate.[15] Among the emerging integrated nonlinear material platforms, aluminum-gallium-arsenide-on-insulator (AlGaAsOI) stands out due to its ultra-high effective nonlinearity.[16,17] AlGaAs possesses a high nonlinear index of 10^{-17} m^2W^{-1},[18] two orders of magnitude lager than that of silicon nitride,[19] which is a widely used platform for soliton generation. Combined with a large linear refractive index of 3.3, the effective nonlinear coefficient up to 660 W^{-1} m^{-1} in third-order nonlinear process has been achieved.[20] Besides, the material bandgap of AlGaAs can be engineered to avoid two-photon absorption at telecom region.[17,18] Large parametric gain,[21] second-harmonic generation,[22] and efficient supercontinuum[23] have been reported in the AlGaAsOI platform, experimentally demonstrating its intense nonlinearity. All these elements make the AlGaAsOI platform an appealing candidate for efficient comb generation.

So far, chaotic micro-combs[24] and coherent platicons (namely bright flat-top pulses)[25] have been demonstrated in the AlGaAsOI platforms with milliwatt-level pump power, easily reachable with chip-integrated lasers.[26] In both cases, the pump is operated in the blue-detuned regime of pump resonances, which is thermally stable.[27] However, DKS generation typically requires transitioning the pump operation from the blue-detuned regime to the red-detuned regime,[28] resulting in abrupt and significant intracavity power variation due to thermal instability characteristic of the red-detuned regime. This poses extreme challenges especially for highly nonlinear material platforms with strong thermo-optic effects such as the AlGaAsOI platform.[29] To facilitate stable soliton generation, one can either minimize the intracavity power variation by optimizing the microresonator design or mitigate thermal instability by reducing thermal effects. The former approach can enhance soliton power and reduce the intracavity power variation but requires an ultrahigh repetition rate and strong anomalous dispersion.[30] Such design constrains result in sparse comb lines and narrow spectral bandwidth, limiting potential applications. Alternatively, cooling

Y. Zhao, C. Ye, Y. Liu, Y. Zhou, K. Yvind, M. Pu
DTU Electro, Department of Electrical and Photonic Engineering
Technical University of Denmark
Kongens Lyngby 2800, Denmark
E-mail: mipu@dtu.dk

The ORCID identification number(s) for the author(s) of this article can be found under https://doi.org/10.1002/lpor.202401223

DOI: 10.1002/lpor.202401223

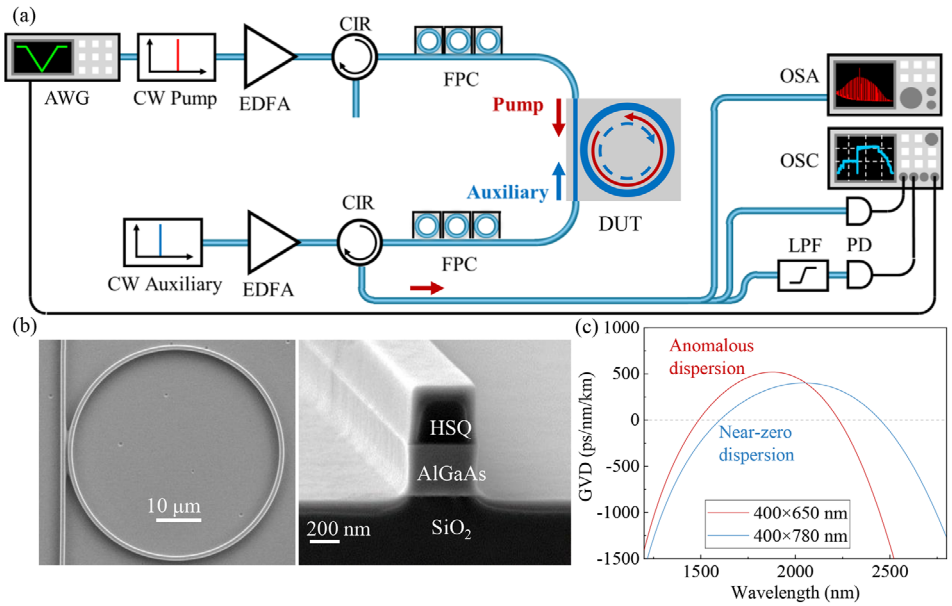

Figure 1. a) Experimental setup for soliton generation via thermal compensation. AWG: arbitrary waveform generator; EDFA: erbium-doped fiber amplifier; CIR: circulator; FPC: fiber polarization controller; DUT: device under test; OSA: optical spectrum analyzer; OSC: oscilloscope; LPF: long-pass filter; PD: photodetector. b) The scanning electron microscopy (SEM) of a 25-μm-radius AlGaAsOI microring resonator and a typical AlGaAsOI waveguide with a sub-micron cross-section dimension. c) Simulated group velocity dispersion (GVD) of 400-nm-thick waveguides with two different widths (red for 650-nm width and blue for 780-nm width).

to cryogenic temperature has been demonstrated to reduce the thermorefractive coefficient of AlGaAs by more than two orders of magnitude, enabling thermally accessible DKS generation.[31] However, room-temperature operation remains desirable for practical application.

To circumvent these restrictions, thermal management via auxiliary laser emerges as an effective method to trigger stable soliton generation.[32] It does not require a complex cryogenic environment and imposes no limitations on the pump power range or the resonator design. While it has been widely adopted in material platforms such as Hydex[33] and silicon nitride,[34] it remains unexplored in platforms like AlGaAsOI, which exhibit orders of magnitude higher thermorefractive coefficients.

Here, we address the thermal management in AlGaAsOI microresonators using an auxiliary laser. By suppressing the thermal resonance shift of an AlGaAsOI microresonator, we demonstrate dual-soliton and single-soliton states in the AlGaAsOI platform at room temperature. Besides, near-zero-dispersion (NZD) solitons are also generated, indicating that the thermal management method is not constrained by dispersion parameters. Based on the stable soliton generation, we explore the influence of intracavity power gradient and show that thermal effects can also be leveraged to extend the soliton existence range (SER). We achieve a large SER up to 37.4 GHz without any active feedback control, ensuring long-term stability for practical applications.

2. Results and Discussion

2.1. Principle

Thermal management is essential for achieving stable soliton generation in AlGaAsOI microresonators. An auxiliary laser serves as an effective tool to regulate intracavity power and mitigate thermal instabilities during the pumping process. The auxiliary laser is tuned into a cavity resonance (the auxiliary resonance) in the blue-detuned regime, while the pump laser remains off-resonance. As the pump wavelength is tuned across the pump resonance into the red-detuned regime, the intracavity power drops abruptly, shifting all resonances toward shorter wavelengths. This effectively cools the cavity and reduces the detuning of the auxiliary laser. This reduced detuning, in turn, increases intracavity heating via the auxiliary resonance, creating a balance between the cooling effect from the pump laser's red-detuned transition and the heating effect from the auxiliary laser. By optimizing the initial detuning and power of the auxiliary laser, a delicate interplay between cooling and heating can be achieved, mitigating intracavity power fluctuations and facilitating stable soliton generation.[32–34] This ensures that the scheme remains unrestricted by the pump power range, dispersion, or free spectral range (FSR).

Figure 1a shows the experimental setup of thermal compensation via auxiliary laser. The pump and auxiliary lasers are amplified and coupled to the opposite edges of the sample using lensed fibers, thus avoiding their interaction and better separating the pump comb from the auxiliary laser. The power of the auxiliary laser is set to a comparable level to the pump laser to compensate for the thermo-optic effect of the microring resonator. Subsequently, the two lasers are extracted through circulators (CIRs). At the pump output, the light is divided into three parts: one is directed to an optical spectrum analyzer (OSA) to observe spectral changes, another is directed to a long pass filter (LPF) to monitor the comb power, and the third is sent to a photodiode (PD) to measure pump transmission. Here, both the pump and auxiliary laser are aligned to the TE polarization. The microresonator is made on

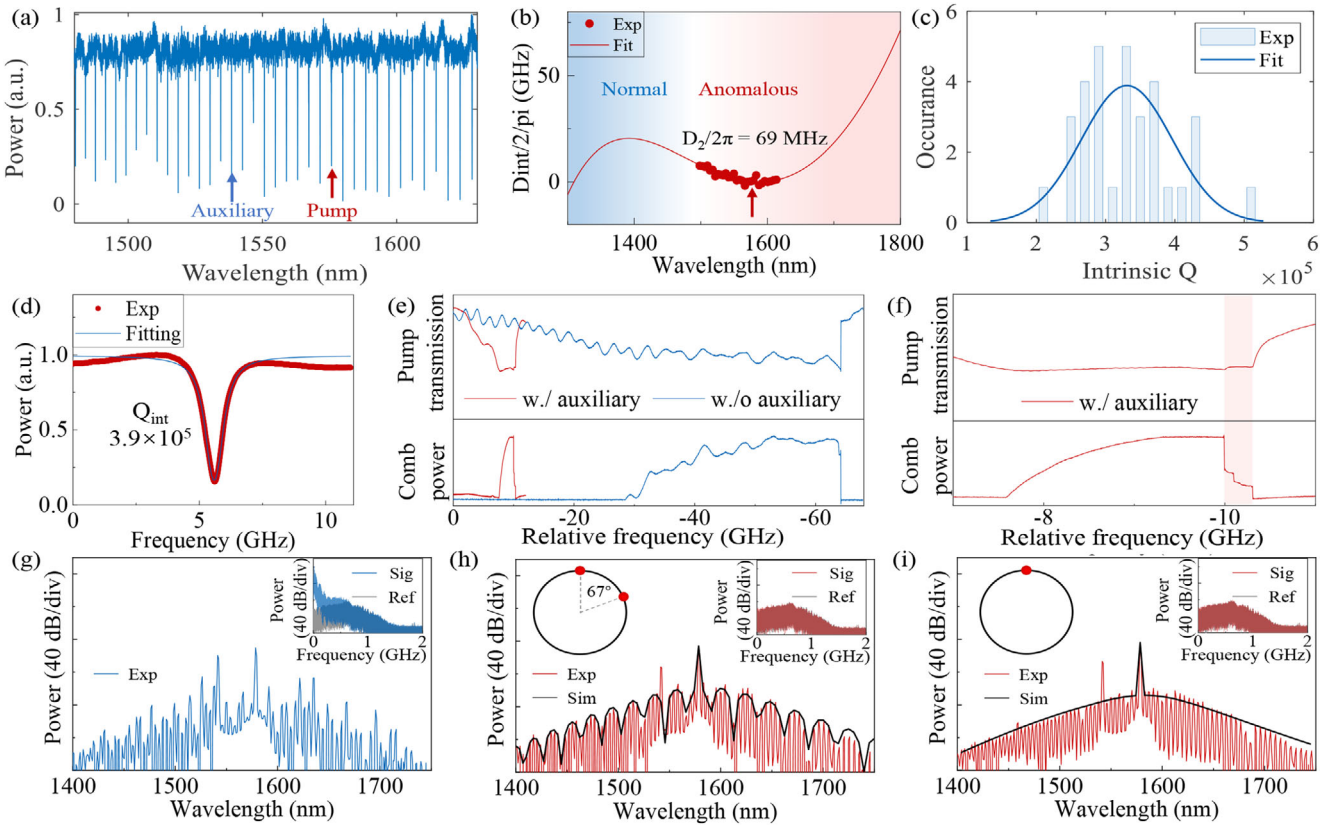

Figure 2. Soliton generation via thermal compensation in AlGaAsOI microring resonator with a cross-section dimension of 400 × 650 nm^2. a) Transmission spectrum of fundamental TE mode. b) Measured integrated dispersion (points) and the corresponding curve fitting (curve), indicating strong anomalous dispersion at pump wavelength 1578 nm. c) Histogram of measured intrinsic Qs for the fundamental TE mode (bars) and corresponding curve fitting (curve). d) A measured resonance similar to the average Q of the device (points) and its Lorentz fitting, showing an intrinsic Q of 3.9 × 10^{-5}. e) Pump transmission and comb power with (red curves) and without (blue curves) auxiliary laser, the thermal resonance shift is significantly suppressed in the former case. f) Enlarged view of results with auxiliary laser in (e), the soliton steps are observed, indicating room-temperature soliton generation. Optical spectra of the g) modulational instability (MI) state, h) dual soliton state, and i) single soliton state. The blue and red curves represent the experimental results, and the black curves represent the simulation results using the Lugiato–Lefever equation (LLE). The top right insets show the low-frequency RF signal, and the top left insets show the relative roundtrip position of the solitons within the microring resonator retrieved from the simulation.

an AlGaAsOI wafer, produced through a wafer bonding and substrate removal process.[35] The device is patterned using electron-beam lithography and dry etching processes.[36] Figure 1b show the scanning electron microscopy (SEM) of a 25-μm-radius AlGaAsOI microring resonator and a typical AlGaAsOI waveguide with a sub-micron cross-sectional dimension.

For DKS generation, anomalous dispersion is required to facilitate phase matching conditions for the parametric oscillation.[28] While AlGaAs exhibits normal material dispersion at telecom bands, the large refractive index contrast between AlGaAs and the silica cladding enables efficient waveguide dispersion engineering. By simply adjusting the waveguide width, we can achieve different dispersion parameters. Based on the finite-element-analysis method, the simulated dispersion profiles are depicted in Figure 1c, where the red curve represents the waveguide cross-section 400 × 650 nm^2 and the blue curve represents 400 × 780 nm^2. At the telecom L-band, strong anomalous dispersion can be secured with 650-nm waveguide width, while near-zero dispersion appears when the width is increased to 780 nm.

2.2. Enabling Soliton Generation by Thermal Management

First, we demonstrate the thermal compensation in a 25-μm-radius AlGaAsOI microring resonator featuring a waveguide cross-section of 400 × 650 nm^2. **Figure** 2a presents the transmission spectrum of the fundamental TE mode, which is obtained using the dispersion characterization setup described in Methods. It shows the FSR of ≈510 GHz. The red and blue arrows indicate the resonances that the pump and auxiliary laser are aligned to. Figure 2b depicts the integrated dispersion (D_{int}) extracted from the transmission data, where the dots indicate the measured result and the curve represents the fitted dispersion profile. The derived 2nd-order dispersion parameter (D_2/π) is 69 MHz at pump resonance (≈1578 nm), inferring strong anomalous dispersion. Notably, there are deviations between the experimental and fitted results, which are induced by the mode coupling in the multi-mode microring resonator.[37] The mode-coupling-induced frequency deviation can be mitigated using a pulley coupler to filter out undesired modes.[38] The intrinsic Q factor (Q_{int})

of each resonance is calculated based on the coupling coefficient and extinction ratio. As shown in Figure 2c, the average intrinsic Q is ≈3.5×10^{-5}, with a typical resonance response depicted in Figure 2d.

Initially, a single pump without the auxiliary laser is employed. Pumped ≈1578 nm with 28-mW on-chip power, the transmission exhibits a distinct thermal triangular spanning over 0.4 nm, illustrated as the blue curves in Figure 2e. The x-axis represents the relative frequency with respect to the starting frequency of the sweep. Subsequently, by tuning the auxiliary laser (35-mW on-chip power) into the resonance ≈1542 nm, the thermal-induced resonance shift is significantly reduced (red curves in Figure 2e)). As can be seen from the enlarged view in Figure 2f, steps are observed in the comb power trace (labeled as red region), indicative of soliton generation. Clearly, the soliton power is much lower than the MI power, which distinguishes our scheme from the previous report.[30] Thereafter, we record the optical and radio-frequency (RF) spectra of frequency combs at different comb states by manually tuning the pump laser into resonance. In the single pump case, we can only observe the MI state with a typical spectrum shown in Figure 2g. The RF spectrum presented in the inset reveals notable RF noise in the low-frequency region. The grey curves in the insets represent the photodetector background, which serves as the reference. Introducing an auxiliary laser enables the generation of various soliton states through manual frequency tuning of the pump laser at room temperature. Figure 2h presents the spectrum of a dual-soliton state, while Figure 2i displays the spectrum of a single-soliton state. They correspond to the soliton steps shown in the comb power trace of Figure 2f. Both RF spectra exhibit low-noise characteristics, indicative of mode-locking. Meanwhile, we perform numerical simulations based on the Lugiato–Lefever equation (LLE) model. Depicted as the black curves in Figure 2h and (i), the simulated spectra match well with the experimental results. The top left insets show the relative roundtrip positions of solitons within the microring resonator retrieved from the simulation.

Soliton generation in the AlGaAs platform has long been a focus due to its ultrahigh nonlinearity, prompting studies dedicated to mitigating the significant thermo-optic challenges. Cooling to cryogenic temperatures can significantly reduce the thermo-optic coefficient, facilitating soliton generation in AlGaAs platforms.[31] However, this method is constrained to a narrow pump power range where soliton states remain thermally accessible, as the thermo-optic coefficient increases sharply with higher pump power. In contrast, the thermal compensation via the auxiliary laser circumvents this limitation by effectively mitigating thermal effects. It offers a more straightforward and stable approach for accessing soliton states in materials with high thermo-optic coefficients.

As the thermal compensation method relaxes the requirements on dispersion and comb spacing for room-temperature soliton combs, we explore NZD soliton generation in an AlGaAsOI microresonator. The waveguide cross-sectional dimension and the radius of the resonator are 400 × 780 nm^2 and 25 μm, respectively. **Figure** 3a depicts the measured integrated dispersion (D_{int}) data (dots) and the fitted profile (curve). The extracted 2nd-order dispersion parameter (D_2/π) is 1 MHz at pump resonance (≈1610 nm), inferring near-zero dispersion. The local dispersion around the pump laser has opposite signs, transitioning from negative values to positive values for D_{int} with wavelength increasing. Here, the pump is set ≈1610 nm and the auxiliary is set ≈1537 nm, both with 30-mW on-chip power. Figures 3b and c present the spectra of a three-soliton and a dual-soliton state, with both RF spectra exhibiting low-noise characteristics. The simulated spectra are in good agreement with the experimental ones, shown as the grey curves. The relative roundtrip positions of multi solitons within the microring resonator are also retrieved and plotted in the top left insets. The simulated temporal waveform of the dual-soliton state is depicted in Figure 3d. The pulses possess multiple peaks, which is the typical feature of NZD solitons.[39–41]

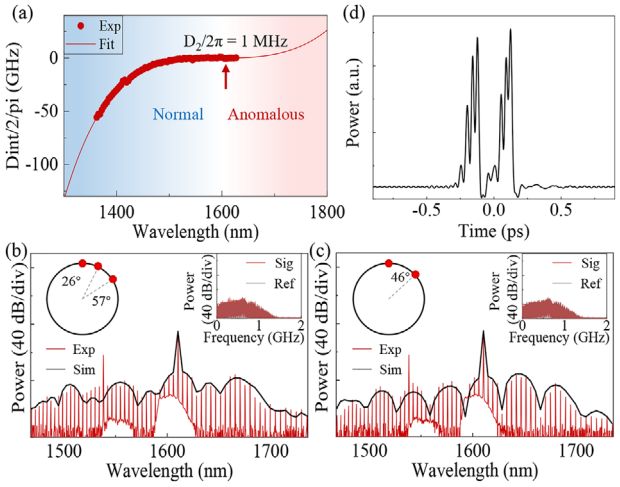

Figure 3. Near-zero-dispersion (NZD) soliton generation in AlGaAs-on-insulator microring resonator with a cross-section dimension of 400 × 780 nm^2. a) Measured integrated dispersion (points) and the corresponding curve fitting (curve), indicating near-zero dispersion at pump wavelength 1610 nm. Optical spectra of the NZD soliton with b) three and c) two solitons. The red curves represent the experimental results, and the black curves represent the simulation results via LLE. The top left insets show the low-frequency RF signal, the top right insets show the relative roundtrip position of the solitons within the microring resonator retrieved from simulation. d) Simulated temporal waveform of the dual-soliton state.

As discussed in previous work,[30] thermally-accessible soliton generation becomes less challenging with higher values of the normalized second-order dispersion parameter D_2/κ, where D_2 denotes the second-order dispersion parameter and κ is the total optical loss rate. By increasing D_2/κ to above 1, the soliton power becomes comparable with MI power, enabling room-temperature soliton generation in AlGaAs platform.[30] However, it necessitates an exceptionally high repetition rate and strong anomalous dispersion. The resulting sparse comb lines and narrow bandwidth severely limit practical applications. Additionally, it does not apply to NZD soliton investigations, which typically accompanies a very low D_2 value. In our case, the values of D_2/κ for NZD soliton is only 0.001, considerably below 1. Nevertheless, the thermal compensation via auxiliary laser bypasses the limitations on both repetition rate and dispersion. Thus, even NZD solitons have been observed using this scheme, broadening the horizons and pushing the boundaries of exploration on AlGaAs platforms.

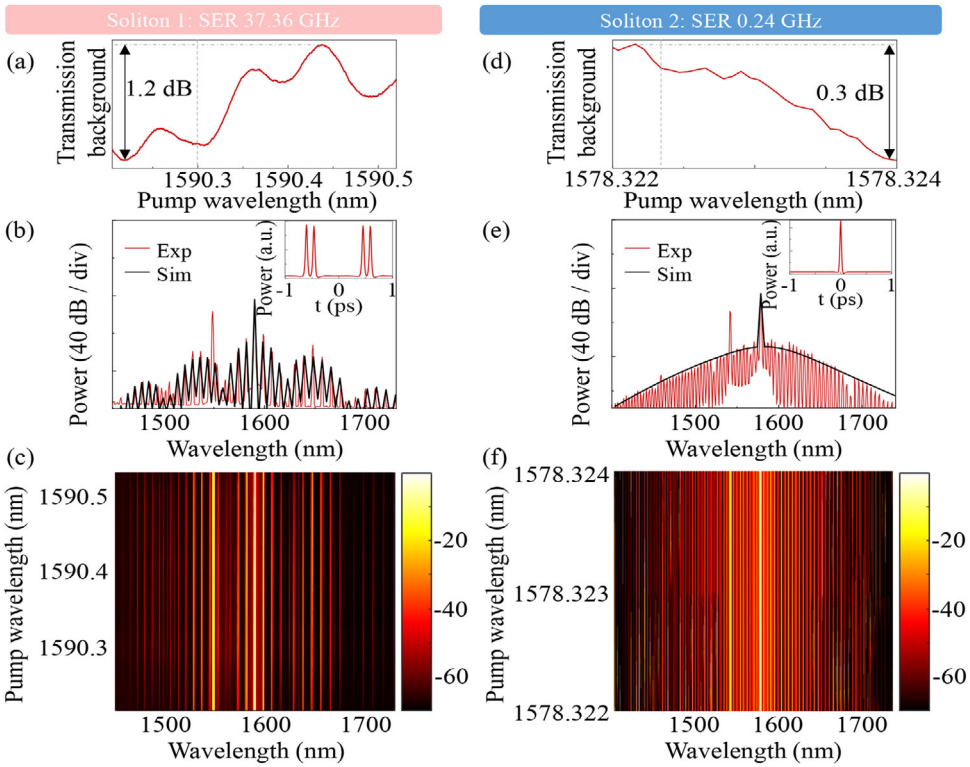

Figure 4. Influence of transmission background fluctuation on soliton existence range (SER). a–c) The overall rising transmission results in an extended existence range of up to 37.3 GHz. d–f) The falling transmission results in a reduced existence range of 0.24 GHz. (a,d) Measured transmission background fluctuations of the bus waveguide. The rising transmission leads to increased intracavity pump power with pump wavelength, which thermally shifts the resonances to longer wavelengths and keeps the effective detuning almost unchanged, thus efficiently extending the SER. In contrast, the falling transmission causes a decreased SER. (b,e) The representative spectra of the two soliton states (red curves) and the corresponding simulation spectral envelope (black curves), the insets show the simulated temporal waveforms. (c,f) Soliton spectral evolution during pump wavelength tuning.

2.3. Extending Soliton Existence Range by Thermal Management

Based on the stable soliton generation by thermal management, we explore the possibility of extending soliton existence range (SER). The thermo-optic effect is generally considered detrimental to bright soliton generation, particularly in materials with a high thermo-optic coefficient, like AlGaAs as discussed previously. However, with proper thermal management, the thermo-optic effect can also be beneficial when the intracavity power increases with the pump wavelength (exhibiting a positive intracavity power gradient). A positive intracavity power gradient within the soliton operation window not only allows the thermo-optic effect to self-stabilize the cavity mode but also induces an additional thermal shift in the pump resonance, effectively extending the SER. The Kerr-induced SER also expands with higher pump power,[42] which further extend the overall SER.

We investigate the influence of different intracavity power gradients on the SER by examining devices with different transmission background fluctuations, employing the same pumping scheme. Specifically, we use two devices with identical waveguide width and height parameters but slightly different bus-to-ring gaps. In the absence of intracavity power gradients, pumping these devices with the same power should yield similar SERs.[43] The transmission background fluctuations for the tested sample primarily originate from factors in the bus waveguide. Facet reflections form a Fabry–Pérot cavity, causing periodic oscillations,[44] while fabrication imperfection, such as local defects or pattern stitching errors, introduces additional reflections.[45] These interferences create arbitrary fluctuations that influence the coupled pump power and can result in positive or negative intracavity power gradients as the pump wavelength sweeps across a cavity resonance.

To compare the SERs, we pump two devices at resonances ≈1590 and 1578 nm, respectively, with the same pump power 30 mW. It is important to note that the auxiliary laser is operated in an under-compensated regime,[33] meaning that the intracavity power variations are still primarily dominated by the pump laser. In **Figure 4a**, the red curve illustrates the transmission background fluctuations measured under cold-cavity condition. These fluctuations, originating from the bus waveguide, remain unaffected by cavity heating during the pumping process.[46] The vertical grey line indicates the point at which the soliton state is reached during forward tuning. After reaching the soliton state, we explore the entire SER by manually tuning the laser forward and backward. The overall rising transmission leads to a positive intracavity power gradient. Although there are several parts in transmission that induces negative intracavity power gradient, their magnitude is minimal enough to keep the effective detuning within the SER, allowing the soliton to be maintained. Figure 4b shows a representative measured spectrum of the soli-

ton state (red curve) alongside the corresponding simulated spectral envelope (black curve), demonstrating a good match. The inset displays the simulated temporal waveform, confirming the formation of a four-soliton state. The whole spectral evolution within the soliton range is recorded in Figure 4b with a pump tuning wavelength step of 5 pm. The spectral shape remains consistent with the low-RF-noise feature when the pump wavelength is tuned from 1590.205 to 1590.520 nm, indicating a large SER of 37.36 GHz. In contrast, other bright soliton demonstrations under similar pump power typically exhibit SERs of less than a few GHz.[15,47] While the large SER is achieved for a multi-soliton state, the scheme is expected to be equally effective for a single soliton state, as the SER is independent of the number of solitons.[43] Due to strong avoided mode crossings in the device, single soliton generation was not achieved.

Figures 4d–f present the results for soliton 2, obtained using the same device as shown in Figure 2. Within the soliton step, the falling transmission results in reduced intracavity pump power as the pump wavelength increases, creating a negative power gradient. This causes blue shifts in the resonances and reduces the Kerr-induced SER. Consequently, the laser-cavity detuning increases more rapidly, further limiting the SER. The optical spectral evolution indicate that the SER for soliton 2 (single soliton) is only 0.24 GHz, which is recorded with a pump wavelength tuning step of 1 pm.

Therefore, the thermo-optic effect can benefit soliton generation concerning the SER. By introducing a positive intracavity power gradient within the soliton operation window, the SER can be efficiently extended, especially in platforms with a large thermo-optic coefficient like AlGaAsOI. It exhibits robustness and operational simplicity without relying on any feedback. The large SER enables significant frequency chirping capability, enhancing ranging resolution in LIDAR applications. To further increase the SER beyond an entire FSR, simultaneous tuning of both pump and auxiliary laser can be employed, along with reducing the FSR. It will facilitate the seamless acquisition of spectrum information by scanning the comb across the FSR, benefiting high-resolution spectroscopy. Although the intracavity power gradient is introduced by the transmission background fluctuation in this work, such a gradient can also be created by introducing an auxiliary cavity mode in the vicinity of pump mode[48] or by intentionally ramping the pump power within the soliton step to extend SERs (see Supporting Information).

3. Conclusion

In conclusion, we demonstrate room-temperature soliton generation in the AlGaAsOI platform using thermal management via an auxiliary laser. This scheme is free from limitations on dispersion or repetition rate, and even NZD soliton states are observed. A large SER is achieved by leveraging the residual thermal effects. With the low operation power, this approach can also be realized in a fully-integrated fashion by combining AlGaAsOI mciroresonators with on-chip lasers using, e.g., heterogeneous integration technology. This advancement is poised to accelerate the adoption of frequency comb sources in practical applications such as LIDAR,[49] data transmission,[5] optical spectroscopy,[2] and optical neural networks.[50]

4. Experimental Section

Q and Dispersion Measurement: To characterize the Q factor and dispersion of AlGaAsOI microring resonators, a free-space cavity was utilized to calibrate frequency since the dispersion in the air was very low. The free-space cavity had a FSR of 100 MHz with a fineness of 1000, resulting in a 100-kHz linewidth, which was much smaller than the resonance linewidth. The probe light was divided into two channels (passing through the AlGaAsOI resonator and the free-space cavity, respectively). At the output, they were detected by two photodetectors and monitored by an oscilloscope to record the transmission trace. The frequency axis was retrieved using the transmission of the free-space cavity. A fiber-loop cavity with a known dispersion value was measured to confirm the reliability of this method. This approach allows for the precise calibration of the resonant frequencies for microresonators.

Supporting Information

Supporting Information is available from the Wiley Online Library or from the author.

Acknowledgements

This work is supported by European Research Council (REFOCUS 853522), Danish National Research Foundation (SPOC ref. DNRF123), VILLUM FONDEN (VIL50469), and Innovationsfonden (GreenCOM 2079-00040B).

Conflict of Interest

The authors declare no conflict of interest.

Data Availability Statement

The data that support the findings of this study are available from the corresponding author upon reasonable request.

Keywords

AlGaAs-on-insulator, dissipative kerr solitons, micro-combs, thermal compensation

Received: August 2, 2024
Revised: December 13, 2024
Published online:

[1] S. A. Diddams, K. Vahala, T. Udem, *Science* **2020**, *369*, 6501.
[2] N. Picqué, T. W. Hänsch, *Nat. Photonics* **2019**, *13*, 146.
[3] A. D. Ludlow, M. M. Boyd, J. Ye, E. Peik, P. O. Schmidt, *Rev. Mod. Phys.* **2015**, *87*, 637.
[4] T. E. Drake, T. C. Briles, J. R. Stone, D. T. Spencer, D. R. Carlson, D. D. Hickstein, Q. Li, D. Westly, K. Srinivasan, S. A. Diddams, S. B. Papp, *Phys. Rev. X* **2019**, *9*, 031023.
[5] H. Hu, F. Da Ros, M. Pu, F. Ye, K. Ingerslev, E. Porto da Silva, M. Nooruzzaman, Y. Amma, Y. Sasaki, T. Mizuno, Y. Miyamoto, L. Ottaviano, E. Semenova, P. Guan, D. Zibar, M. Galili, K. Yvind, T. Morioka, L. K. Oxenløwe, *Nat. Photonics* **2018**, *12*, 469.
[6] M. G. Suh, K. J. Vahala, *Science* **2018**, *359*, 884.

[7] T. J. Kippenberg, A. L. Gaeta, M. Lipson, M. L. Gorodetsky, *Science* **2018**, *361*, 6402.
[8] A. L. Gaeta, M. Lipson, T. J. Kippenberg, *Nat. Photonics* **2019**, *13*, 158.
[9] L. Chang, S. Liu, J. E. Bowers, *Nat. Photonics* **2022**, *16*, 95.
[10] V. Brasch, M. Geiselmann, T. Herr, G. Lihachev, M. H. P. Pfeiffer, M. L. Gorodetsky, T. J. Kippenberg, *Science* **2016**, *351*, 357.
[11] X. Yi, M.-G. Suh, K. Y. Yang, Q.-F. Yang, K. Vahala, *Optica* **2015**, *2*, 1078.
[12] X. Liu, Z. Gong, A. W. Bruch, J. B. Surya, J. Lu, H. X. Tang, *Nat. Commun.* **2021**, *12*, 5428.
[13] M. A. Guidry, D. M. Lukin, K. Y. Yang, R. Trivedi, J. Vučković, *Nat. Photonics* **2021**, *16*, 52.
[14] D. Xia, Z. Yang, P. Zeng, B. Zhang, J. Wu, Z. Wang, J. Zhao, J. Huang, L. Luo, D. Liu, S. Yang, H. Guo, Z. Li, *Laser Photon. Rev.* **2023**, *17*, 2200219.
[15] Y. He, Q.-F. Yang, J. Ling, R. Luo, H. Liang, M. Li, B. Shen, H. Wang, K. Vahala, Q. Lin, *Optica* **2019**, *6*, 1138.
[16] S. T. Ho, C. E. Soccolich, M. N. Islam, W. S. Hobson, A. F. J. Levi, R. E. Slusher, *Appl. Phys. Lett.* **1991**, *59*, 2558.
[17] J. S. Aitchison, D. C. Hutchings, J. U. Kang, G. I. Stegeman, A. Villeneuve, *IEEE J. Quantum Electron.* **1997**, *33*, 341.
[18] P. Apiratikul, C. J. K. Richardson, J. J. Wathen, G. M. Carter, T. E. Murphy, G. A. Porkolab, *Opt. Lett.* **2014**, *39*, 3161.
[19] K. Ikeda, R. E. Saperstein, N. Alic, Y. Fainman, V. R. Almeida, C. A. Barrios, R. R. Panepucci, M. Lipson, *Opt. Express* **2008**, *16*, 12987.
[20] M. Pu, L. Ottaviano, E. Semenova, K. Yvind, *Optica* **2016**, *3*, 823.
[21] Y. Zhao, C. Kim, Y. Zheng, C. Ye, Y. Zhou, K. Yvind, M. Pu, in *Conf. on Lasers and Electro-Optics*, Optica Publishing Group, Washington, DC, USA **2022**, Paper SM4O.6.
[22] M. Sorel, M. Clerici, M. Kues, S. May, *Opt. Lett.* **2019**, *44*, 1339.
[23] B. Kuyken, M. Billet, F. Leo, K. Yvind, M. Pu, *Opt. Lett.* **2020**, *45*, 603.
[24] L. Chang, W. Xie, H. Shu, Q. F. Yang, B. Shen, A. Boes, J. D. Peters, W. Jin, C. Xiang, S. Liu, G. Moille, S. P. Yu, X. Wang, K. Srinivasan, S. B. Papp, K. Vahala, J. E. Bowers, *Nat. Commun.* **2020**, *11*, 1331.
[25] H. Shu, L. Chang, Y. Tao, B. Shen, W. Xie, M. Jin, A. Netherton, Z. Tao, X. Zhang, R. Chen, B. Bai, J. Qin, S. Yu, X. Wang, J. E. Bowers, *Nature* **2022**, *605*, 457.
[26] C. Xiang, W. Jin, D. Huang, M. A. Tran, J. Guo, Y. Wan, W. Xie, G. Kurczveil, A. M. Netherton, D. Liang, H. Rong, J. E. Bowers, *IEEE J. Sel. Top. Quantum Electron.* **2022**, *28*, 3323.
[27] T. Carmon, L. Yang, K. J. Vahala, *Opt. Express* **2004**, *12*, 4742.
[28] T. Herr, V. Brasch, J. D. Jost, C. Y. Wang, N. M. Kondratiev, M. L. Gorodetsky, T. J. Kippenberg, *Nat. Photonics* **2014**, *8*, 145.
[29] M. Gao, Q. F. Yang, Q. X. Ji, H. Wang, L. Wu, B. Shen, J. Liu, G. Huang, L. Chang, W. Xie, S. P. Yu, S. B. Papp, J. E. Bowers, T. J. Kippenberg, K. J. Vahala, *Nat. Commun.* **2022**, *13*, 3323.
[30] L. Wu, W. Xie, C. Xiang, L. Chang, Y. Yu, H. J. Chen, Y. Yamamoto, J. E. Bowers, K. J. Vahala, M. G. Suh, *Opt. Lett.* **2023**, *48*, 3853.
[31] G. Moille, L. Chang, W. Xie, A. Rao, X. Lu, M. Davanço, J. E. Bowers, K. Srinivasan, G. Moille, A. Rao, X. Lu, M. Davanço, K. Srinivasan, L. Chang, W. Xie, J. E. Bowers, *Laser Photon. Rev.* **2020**, *14*, 2000022.
[32] S. Zhang, J. M. Silver, L. Del Bino, F. Copie, M. T. M. Woodley, G. N. Ghalanos, A. Ø. Svela, N. Moroney, P. Del'Haye, *Optica* **2019**, *6*, 206.
[33] Y. Zhao, L. Chen, C. Zhang, W. Wang, H. Hu, R. Wang, X. Wang, S. T. Chu, B. Little, W. Zhang, X. Zhang, *Laser Photon. Rev.* **2021**, *15*, 2100264.
[34] H. Zhou, Y. Geng, W. Cui, S. W. Huang, Q. Zhou, K. Qiu, C. W. Wong, *Light Sci. Appl.* **2019**, *8*, 50.
[35] L. Ottaviano, M. Pu, E. Semenova, K. Yvind, *Opt. Lett.* **2016**, *41*, 3996.
[36] C. Kim, C. Ye, Y. Zheng, E. Semenova, K. Yvind, M. Pu, *IEEE J. Sel. Top. Quantum Electron.* **2022**, *29*, 5900214.
[37] C. Kim, K. Yvind, M. Pu, *Opt. Lett.* **2021**, *46*, 3508.
[38] C. Ye, Y. Liu, Y. Zhou, Y. Zhao, Y. Zheng, C. Kim, L. K. Oxenlowe, K. Yvind, M. Pu, *IEEE J. Sel. Top. Quantum Electron.* **2024**, *30*, 5100111.
[39] M. H. Anderson, W. Weng, G. Lihachev, A. Tikan, J. Liu, T. J. Kippenberg, *Nat. Commun.* **2022**, *13*, 4764.
[40] Q.-X. Ji, W. Jin, W. Jin, L. Wu, Y. Yu, Z. Yuan, W. Zhang, M. Gao, B. Li, H. Wang, H. Wang, C. Xiang, J. Guo, A. Feshali, M. Paniccia, V. S. Ilchenko, A. B. Matsko, J. E. Bowers, K. J. Vahala, *Opt.* **2023**, *10*, 279.
[41] Z. Xiao, T. Li, M. Cai, H. Zhang, Y. Huang, C. Li, B. Yao, K. Wu, J. Chen, *Light Sci. Appl.* **2023**, *12*, 33.
[42] Ó. B. Helgason, M. Girardi, Z. Ye, F. Lei, J. Schröder, V. Torres-Company, *Nat. Photonics* **2023**, *17*, 992.
[43] H. Guo, M. Karpov, E. Lucas, A. Kordts, M. H. P. Pfeiffer, V. Brasch, G. Lihachev, V. E. Lobanov, M. L. Gorodetsky, T. J. Kippenberg, *Nat. Phys.* **2017**, *13*, 94.
[44] L. Jia, M. Yu, J. Song, T.-Y. Liow, X. Luo, X. Tu, S.-C. Koh, G. Lo, Q. Fang, *Opt. Express* **2014**, *22*, 23652.
[45] D. Melati, F. Morichetti, A. Melloni, *Adv. Opt. Photonics* **2014**, *6*, 156.
[46] Y. Zheng, M. Pu, H. K. Sahoo, E. Semenova, K. Yvind, *J. Light. Technol.* **2019**, *37*, 868.
[47] S.-P. Yu, D. C. Cole, H. Jung, G. T. Moille, K. Srinivasan, S. B. Papp, *Nat. Photonics* **2021**, *15*, 461.
[48] Q. Li, T. C. Briles, D. A. Westly, T. E. Drake, J. R. Stone, B. R. Ilic, S. A. Diddams, S. B. Papp, K. Srinivasan, *Optica* **2017**, *4*, 193.
[49] J. Riemensberger, A. Lukashchuk, M. Karpov, W. Weng, E. Lucas, J. Liu, T. J. Kippenberg, *Nat.* **2020**, *581*, 164.
[50] J. Feldmann, N. Youngblood, M. Karpov, H. Gehring, X. Li, M. Stappers, M. L. Gallo, X. Fu, A. Lukashchuk, A. S. Raja, J. Liu, C. D. Wright, A. Sebastian, T. J. Kippenberg, W. H. P. Pernice, H. Bhaskaran, *Nature* **2021**, *589*, 52.